Chapter 8 – EFFECTS OF LOW- AND HIGH-FIDELITY SOLVERS ON HULL-FORM OPTIMIZATION

Matteo Diez[1], Andrea Serani[1], Giovanni Fasano[2], Giampaolo Liuzzi[3], Stefano Lucidi[4], Umberto Iemma[5], Emilio F. Campana[1], Frederick Stern[6]

[1] CNR-INSEAN, National Research Council-Marine Technology Research Institute, Rome, Italy
[2] Department of Management, Ca' Foscari University of Venice, Venice, Italy
[3] CNR-IASI, National Research Council-Inst. for Systems Analysis and Computer Science, Rome, Italy
[4] Dep. of Computer, Control, and Management Engineering "A. Ruberti", Sapienza University, Rome, Italy
[5] Department of Engineering, Roma Tre University, Rome, Italy
[6] The University of Iowa, IIHR-Hydroscience and Engineering, Iowa City, IA, USA

8.1   ABSTRACT

This chapter investigates on the effects of the hydrodynamic solver on the multi-objective hull-form optimization of the DTMB 5415 model in calm water. Potential flow and Reynolds-averaged Navier–Stokes (RANS) solvers are compared. The former is formulated and implemented using two linearization approaches (Kelvin and Dawson), combined with two methods for the wave resistance. The Pareto fronts for the reduction of the resistance at two speeds are obtained by a multi-objective deterministic particle swarm optimization and are significantly affected by the potential flow formulation. A correlation analysis with RANS is shown, in order to suggest the most effective potential flow formulation for the present case. Finally, a RANS-based metamodel is used for a single-objective optimization, for the calm water resistance at Fr=0.25, using global and global/local hybrid optimization algorithms.

8.2   LIST OF FIGURES

8.3   LIST OF TABLES

8.4   INTRODUCTION

High-fidelity solvers (such as Reynolds-averaged Navier–Stokes, RANS) have shown their capability to provide accurate solutions to the design problem [1]. Their computational cost is still a critical issue in simulation-based design optimization (SBDO). For this reason, metamodels and variable-fidelity approaches, based on low- and high-fidelity solvers, have been developed and applied to reduce the computational time and cost of the SBDO. Low-fidelity solvers (such as potential flow, PF) have been applied to identify suitable design spaces for RANS-based optimization [2]. Identifying the proper trend of the design objective versus the design variables often represents a critical issue for a low-fidelity solver, especially when large design modifications are involved. The choice of a low-fidelity solver within SBDO represents a critical issue and should be carefully justified, considering the trade-off between computational efficiency and solution accuracy.

The objective of this chapter is to investigate the effects of the hydrodynamic solver on the results of a multi-objective SBDO in ship hydrodynamics. Two different linearization approaches for the PF solver are compared, namely Kelvin and Dawson [3], combined with two different methodologies for the calculation of the wave resistance: a standard pressure integral over the body surface and the transversal wave cut method [4]. The chapter then presents a sensitivity analysis of the hydrodynamic performance using RANS, in order to compare and correlate PF and RANS trends, and evaluate benefits and drawbacks of the PF formulations within SBDO.

The application presented is the hull-form optimization of the DTMB 5415 model. In the present chapter, a multi-objective SBDO example is shown, aimed at the reduction of the total resistance at 18 kn and 30 kn, corresponding to Froude number Fr=0.25 and Fr=0.41, respectively. The case considered is a 2 DOF problem with free-surface. The model advances in calm water and is free to heave (stationary sinkage) and pitch (stationary trim). A linear expansion of orthogonal basis function is used for the shape modification. Specifically, two sets of orthogonal functions are applied for the modification of the hull and the sonar dome shapes, and controlled by a total number of design variables $N = 6$. A multi-objective extension of the deterministic particle swarm optimization algorithm (MODPSO) is used [5]. The constraints include fixed displacement and fixed length between perpendiculars, along with a ±5% maximum variation of beam and draft, and a reserved volume for the sonar in the dome. PF simulations are conducted using the code WARP (WAve Resistance Program), developed at INSEAN. RANS investigations are performed using the CFDShip-Iowa code [6], developed at the University of Iowa.

Finally, a single-objective high-fidelity optimization for the reduction of the model scale total resistance coefficient of DTMB 5415 is performed using RANS. Four global and global/local optimization algorithm have been applied on a RANS-based metamodel. The design space is composed by a total number of $N = 11$ design variables, that are the result of a dimensionality reduction analysis, based on the Karhunen-Loève expansion (KLE) [7]. Geometrical and functional constraints are the same of the multi-objective problem.

The chapter is organized as follows. Section 8.5 presents the low- vs high-fidelity multi-objective optimization in calm water at Fr=0.25 and Fr=0.41, comparing PF and RANS. Section 8.6 presents the high-fidelity single-objective optimization in calm water at Fr=0.25, using a RANS-based metamodel. The final conclusions are included in Section 8.7.

Further details of the current results have been published in [8] [9] [10].

8.5 LOW- VS HIGH-FIDELITY MULTI-OBJECTIVE OPTIMIZATION

In this section, the effects of the potential flow on the multi-objective optimization of the DTMB 5415 in calm water are investigated and the results compared to RANS-based solutions.

8.5.1 Geometry, Conditions, and Optimization Problem Formulation

Figure 8-1 shows the geometry of a 5.720 m length DTMB 5415 model used for towing tank experiments, as seen at INSEAN [11]. The main particulars of the full scale model and test conditions are summarized in Table 8-1 and Table 8-2, respectively.

Figure 8-1: A 5.720 m length model of the DTMB 5415 (CNR-INSEAN model 2340).

Table 8-1: DTMB 5415 model main particulars (full scale).

Description	Symbol	Units	Value
Displacement	∇	tonnes	8636
Length between perpendiculars	LBP	m	142.0
Beam	B	m	18.90
Draft	T	m	6.160
Longitudinal center of gravity	LCG	m	71.60
Vertical center of gravity	VCG	m	1.390

Table 8-2: Test conditions (full scale).

Description	Symbol	Units	Value
Speed	U_1, U_2	kn	18.00, 30.00
Water density	ρ	kg/m^3	998.5
Kinematic viscosity	ν	m^2/s	$1.09 \cdot 10^{-6}$
Gravity acceleration	g	m/s^2	9.803

The multi-objective problem is defined as

$$\begin{aligned} \text{minimize} \quad & f_1(\mathbf{x}), f_2(\mathbf{x}) \\ \text{subject to} \quad & \mathbf{l} \le \mathbf{x} \le \mathbf{u} \\ \text{and to} \quad & g_k(\mathbf{x}) \le 0, \quad k = 1, \dots, N_g \end{aligned} \quad (1)$$

where f_1 and f_2 are the total resistance (R_T) in calm water at Fr=0.25 and Fr=0.41; $\mathbf{x}$ is the design variable vector; $\mathbf{l}$ and $\mathbf{u}$ are the design variables lower and upper bound vectors, and g_k are the geometrical constraints. These include fixed length between perpendiculars (LBP=142.0 m), fixed displacement (∇=8636 tonnes), beam and draft variation within ±5% of the original values (B=18.90 m; T=6.160 m), reserved volume in the dome for the sonar (4.9 m diameter; 1.7 m height).

8.5.2   CFD, Design Modification, and Optimization Methods

The hydrodynamic solvers used are described in the following. The simulation setups are also briefly included.

8.5.2.1 Potential Flow Formulations and Simulation Setup

Wave resistance computations are based on the linear PF theory (e.g., [1]). The simplest linear formulation (Kelvin linearization) is obtained by assuming that the actual flow is slightly perturbed from the free stream, and its potential function is given by $\phi = Ux + \tilde{\varphi}$, which provides the Neumann-Kelvin (NK) problem for the Laplace equation. A further linearization, suggested by [12], is based on the assumption that the flow near the body is perturbed around the double model (DM) flow, and its potential function is given by $\phi = Ux + \varphi_d + \tilde{\varphi}$. NK is usually reasonable for slender bodies and high speeds, whereas DM is usually more suitable for wider bodies and low speeds. Herein, once the flow is solved the wave resistance is evaluated by both a pressure integral over the body surface and the transverse wave cut method [4]. The frictional resistance is estimated using a flat-plate approximation, based on the local Reynolds number [13]. The steady 2 DOF (sinkage and trim) equilibrium is achieved by iteration of the flow solver and the body equation of motion.

The solver used is WARP, and the linearization and the wave resistance estimation methods are combined, producing four different PF formulations: (a) Neumann-Kelvin with pressure integral method (NK-PI), (b) Neumann-Kelvin with transverse wave cut method (NK-WC), (c) double model linearization with pressure integral method (DM-PI), and (d) double model linearization with transverse wave cut method (DM-WC). Numerical implementation and validation of the numerical solvers are given by [1].

Simulations are performed for the right demi-hull, taking advantage of symmetry about the *xz*-plane. The computational domain for the free-surface is defined within 1 hull length upstream, 3 lengths downstream and 1.5 lengths aside. Table 8-3 summarize the associated panel grid used (see Figure 8-2), and guarantee solution convergence.

(a) Body grid   (b) Free-surface grid
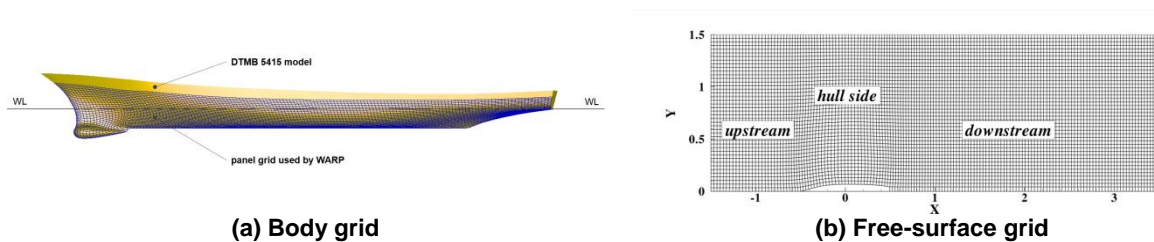
Figure 8-2: Computational panel grid for WARP.

Table 8-3: Panel grid used for WARP.

Hull	Free surface			Total
	Upstream	Hull side	Downstream	
150×30	30×44	30×44	90×44	11k

8.5.2.2 RANS Solver and Simulation Setup

RANS simulations are performed with the CFDShip-Iowa V4.5 code [6], which has the capability of a 6 DOF simulation and has been developed at IIHR-Hydroscience & Engineering over the past 25 years, for ship hydrodynamics applications. The SST blended $k - \varepsilon / k - \omega$ turbulent model is selected. The free-surface location is predicted by a single phase level set method. A second order upwind scheme is used to discretize the convective terms of momentum equations. For a high performance parallel computing, an MPI-based domain decomposition approach is used, where each decomposed block is mapped to one processor. The code SUGGAR runs as a separate process from the flow solver to compute interpolation coefficients for the overset grid, which enables CFDShip-Iowa to take care of 6 DOF with a motion controller at every time step. Only 2 DOFs are considered in the current study. Table 8-4 summarizes the associated volume grid used (see Figure 8-3).

(a) Background   (b) Boundary layer
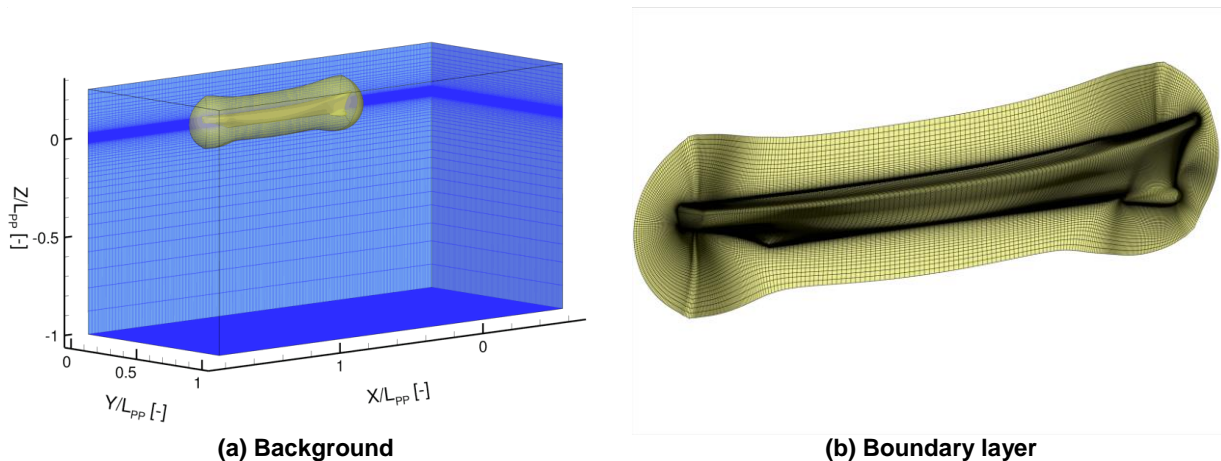
Figure 8-3: Computational volume grid for CFDShip-Iowa.

Table 8-4: Volume grid used for CFDShip-Iowa.

Background	Boundary layer	Total
$227 \times 155 \times 115$	$243 \times 71 \times 115$	6M

8.5.2.3 Hull-form Modification Method

An orthogonal representation of the shape modification is used [8], since it is more efficient in the context of shape design optimization [7]. For details of equations and numerical implementations the reader is referred to Chapter 3 (the design space used correspond to C.1).

8.5.2.4 Multi-objective Deterministic Particle Swarm Optimization

Details, formulation, and setup of the multi-objective deterministic particle swarm optimization algorithm [5] used can be found in Chapter 3. A maximum number of function evaluations is set equal to 1,536, which corresponds to 256*N*, where *N* is the number of design variables.

8.5.3   Numerical Results

A preliminary validation of PF and RANS simulations versus experimental (EFD) data collected at INSEAN [14] is shown in Figure 8-4 for the original DTMB 5415 model (LBP=5.720 m). A reasonable trend is shown, especially for low Froude numbers, of total resistance coefficient (C_T, Figure 8-4a), sinkage (σ, Figure 8-4b), and trim (τ, Figure 8-4c) for all formulations but NK-PI for total resistance and NK for sinkage.
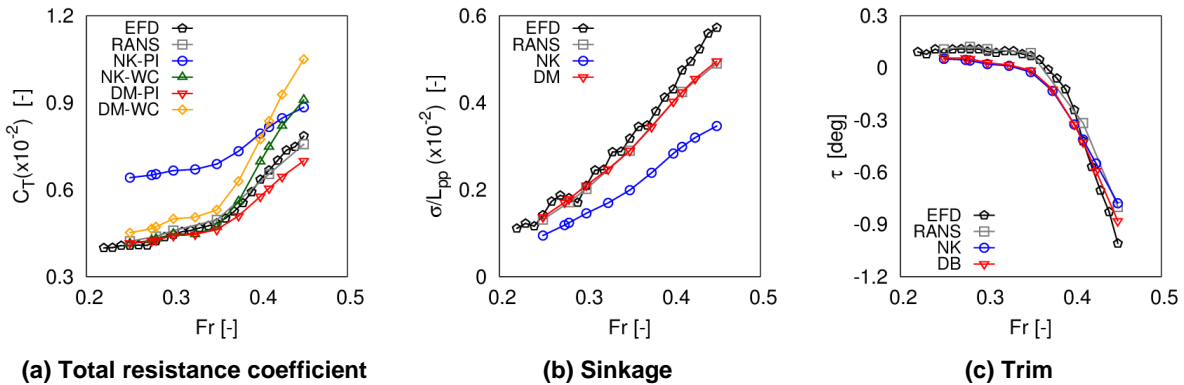
Figure 8-4: Model scale validation for PF and RANS.

A preliminary sensitivity analysis in full scale (LBP=142.0 m) for each design variable is presented in Figure 8-5, showing the associated objective function reduction, Δf_1 and Δf_2. Unfeasible designs are not reported in the plot. Changes in Δf_1 and Δf_2 are found overall significant with each PF formulation. It may be noted how Δf_1 and Δf_2 versus x_1 with NK-PI show an opposite trend compared to the other formulations.
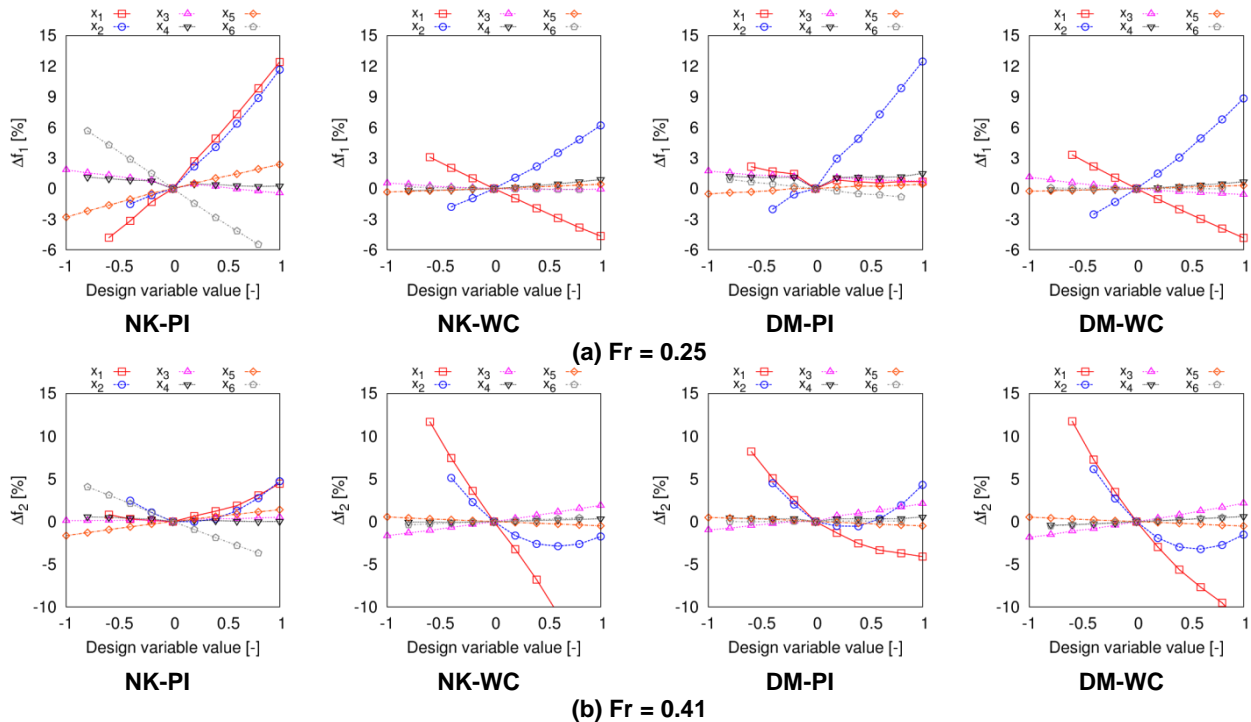
Figure 8-5: Preliminary sensitivity analysis with PF.

Figure 8-6a shows the Pareto front obtained with each PF formulation. The design variable values of the Pareto front solutions are shown in Figure 8-6b. The best compromise solution between the two objective functions (minimum $\Delta f_1 + \Delta f_2$) is selected, and the corresponding design variable values are shown in Figure 8-6c. Different formulations identify different optimal solutions, as also shown in Figure 8-7.

Table 8-5: Hull-form optimization results (selected hulls).

| PF formulation	x_1	x_2	x_3	x_4	x_5	x_6	Δf_1 %	Δf_2 %
NK-PI	-1.000	0.239	-0.538	0.458	-1.000	1.000	-16.5	-4.9
NK-WC	0.997	0.325	-0.862	-0.917	-0.136	-0.999	-2.5	-23.0
DM-PI	0.880	-0.358	0.077	-0.505	1.000	0.799	-4.3	-1.1
DM-WC	1.000	0.294	0.399	-0.732	0.427	-1.000	-3.1	-16.3

(a) Pareto fronts (f_1; f_2)   **(b) Pareto fronts (x)**   **(c) Selected design variables**
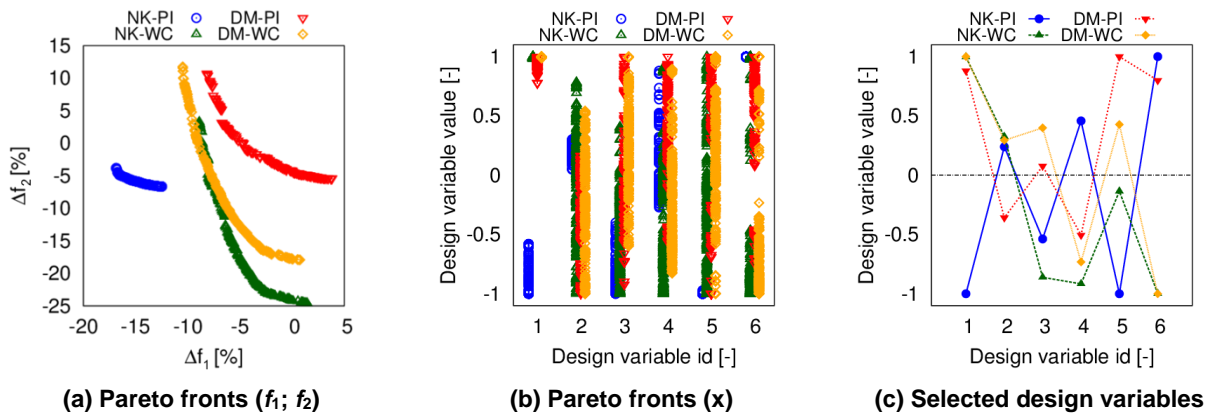
Figure 8-6: Multi-objective hull-form optimization results.

Table 8-5 shows the objective function reduction achieved with each PF formulation, for the selected optimal solutions. Except for NK-PI, the reduction of the resistance is consistent with the reduction of the wave elevation pattern, both in terms of transverse and diverging Kelvin waves, for both Fr=0.25 (see Figure 8-8a) and Fr=0.41 (see Figure 8-8b). Figure 8-9 shows the pressure field of the optimized hulls compared to the original, showing a better pressure recovery towards the stern (except for NK-PI).

(a) NK-PI   **(b) NK-WC**   **(c) DM-PI**   **(d) DM-WC**

Figure 8-7: Selected optimal shapes, compared to the original.

(a) Fr = 0.25

(b) Fr = 0.41
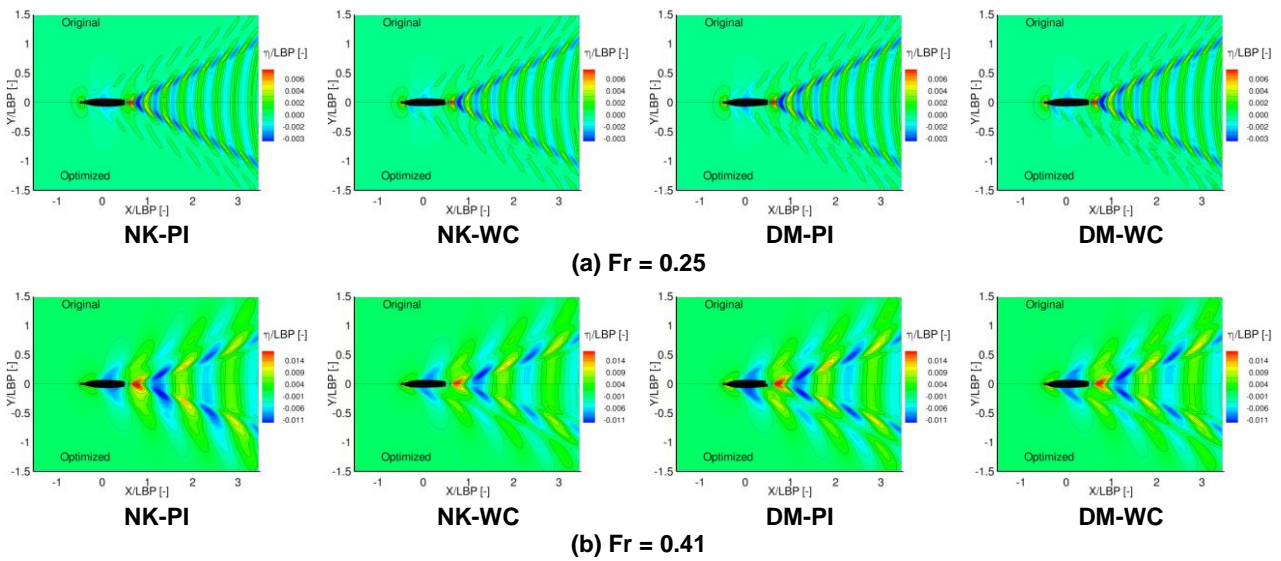
Figure 8-8: Wave elevation of the selected optimal hulls, compared with the original.

(a) Fr = 0.25

(b) Fr = 0.41

Figure 8-9: Pressure of the selected optimal hulls, compared with the original.

The heterogeneity of the results obtained with the different PF formulations motivates a further investigation by the RANS solver. 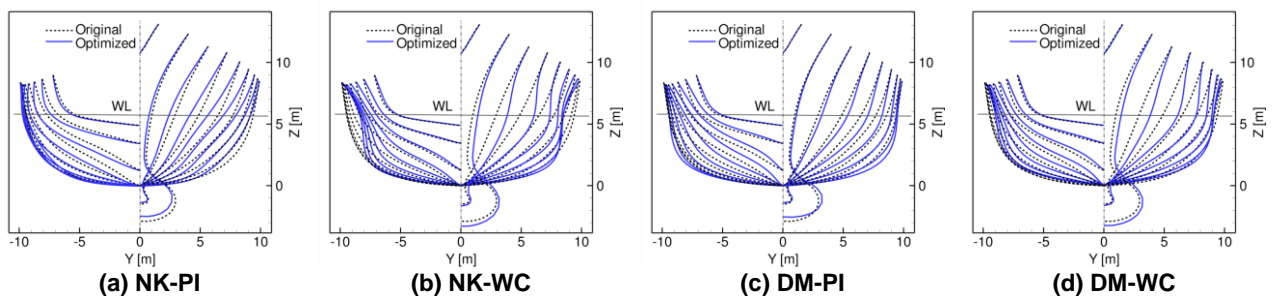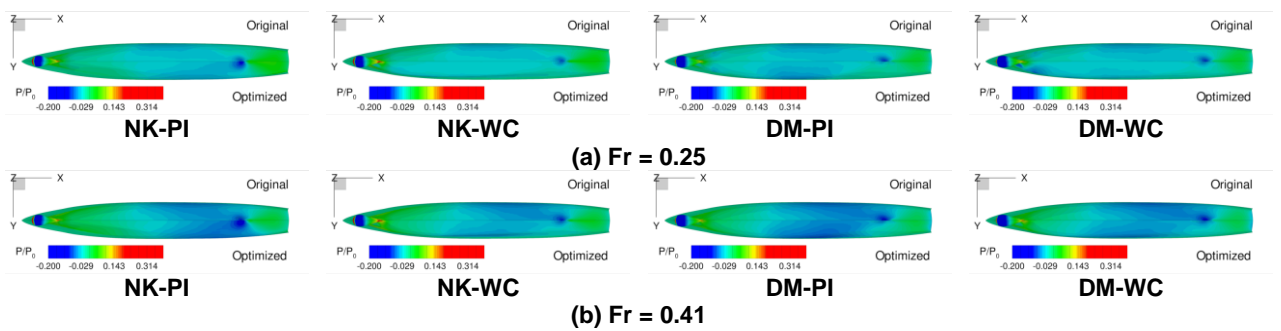Specifically, the sensitivity analysis (in model scale, LBP=5.720 m) at Fr=0.25 obtained with the PF formulations is compared to RANS for each design variable, as shown in Figure 8-10. The RANS solutions show several differences compared to the PF formulations. In particular, the trend of the total resistance coefficient is captured only by NK-PI for x_1, and by all the PF formulations for x_2 and x_3, whereas x_4, x_5, and x_6 trends are not in agreement with RANS, even if the results are likely within the solution's uncertainty band. Moreover, Figure 8-11 shows the error or difference (ε %) between PF formulations and RANS, for each design variable. The NK-PI formulation has the higher error, although almost constant. Table 8-6 summarizes the average absolute errors ($\overline{|\varepsilon|}$%) of the PF formulations. Specifically, the NK-WC and DM-PI formulations have the lowest average error, close to 2%. The analysis of the Pearson's correlation coefficient (r) between PF and RANS results (see Table 8-7) shows a good correlation between NK-PI and RANS for x_1, x_2, x_3, and x_5. The other PF formulations have a good correlation for x_2 and x_3, whereas the correlation for x_4 and x_6 is poor overall, indicating a totally different trend in some case. NK-PI has the better correlation with RANS solutions on average.
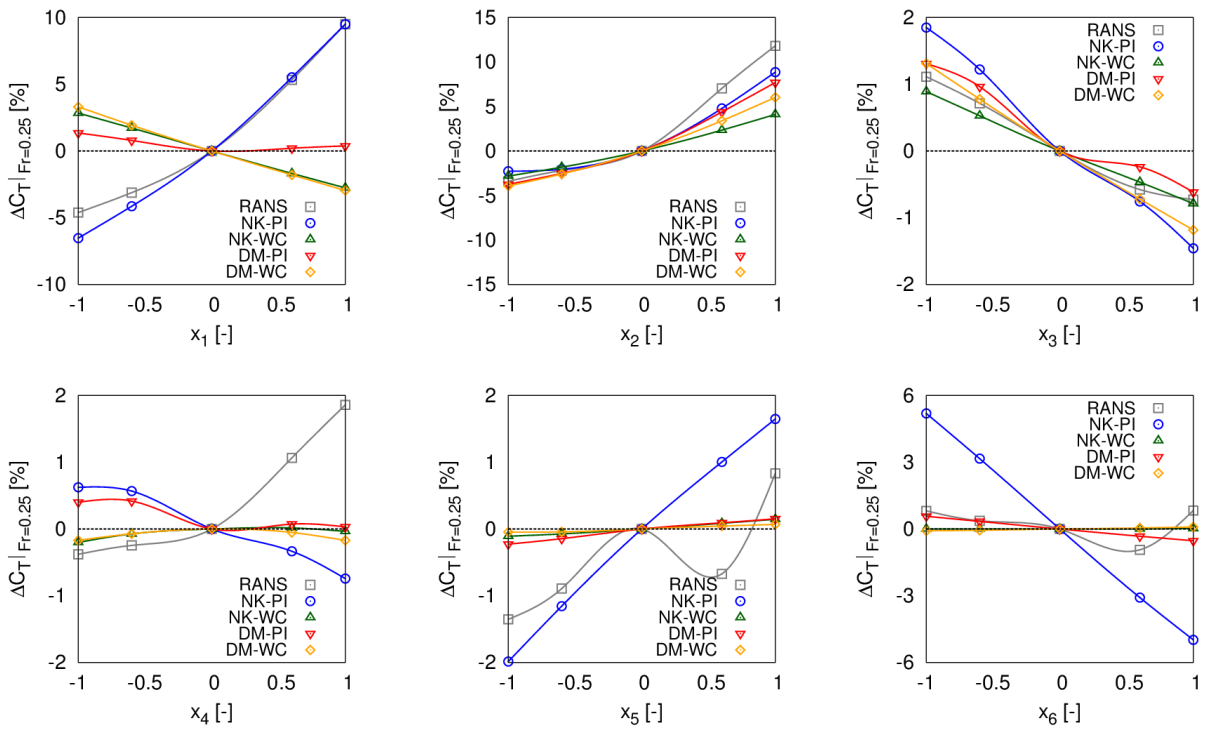
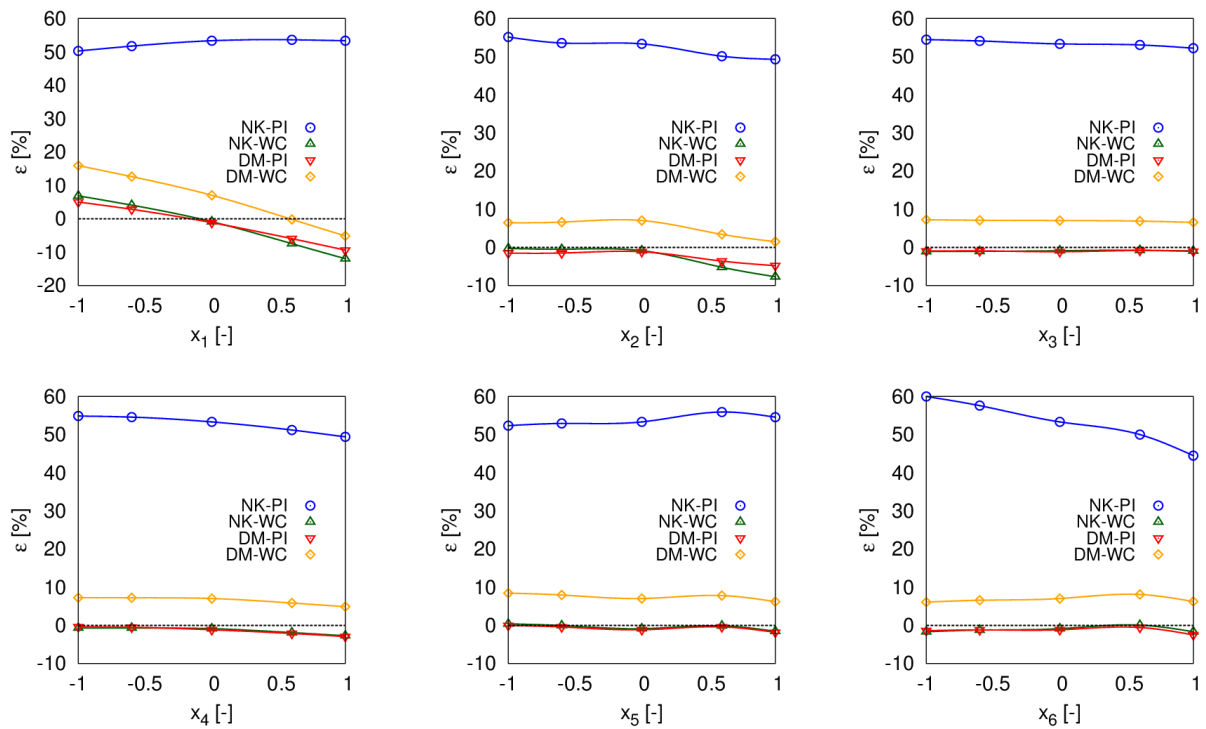**Figure 8-10: Comparison of trends between PF and RANS at Fr=0.25.**

Figure 8-11: PF error compared to RANS at Fr=0.25

Table 8-6: PF average error compared to RANS.

PF formulation	$\overline{\lvert \varepsilon \rvert}_{x_1}$ %	$\overline{\lvert \varepsilon \rvert}_{x_2}$ %	$\overline{\lvert \varepsilon \rvert}_{x_3}$ %	$\overline{\lvert \varepsilon \rvert}_{x_4}$ %	$\overline{\lvert \varepsilon \rvert}_{x_5}$ %	$\overline{\lvert \varepsilon \rvert}_{x_6}$ %	Average%
NK-PI	52.5	52.3	53.4	52.7	53.8	53.1	53.0
NK-WC	6.3	2.9	0.9	1.4	0.6	1.1	2.2
DM-PI	4.9	2.5	1.0	1.4	0.8	1.4	2.0
DM-WC	8.2	5.0	7.0	6.5	7.5	6.8	6.8

Table 8-7: Pearson product-moment correlation coefficient between PF and RANS from Figure 8-11.

PF formulation	r_{x_1} [-]	r_{x_2} [-]	r_{x_3} [-]	r_{x_4} [-]	r_{x_5} [-]	r_{x_6} [-]	Average [-]
NK-PI	0.997	0.998	0.993	-0.956	0.826	0.331	0.531
NK-WC	-0.983	0.985	0.994	0.538	0.818	0.482	0.472
DM-PI	-0.622	0.995	0.987	-0.679	0.827	0.335	0.307
DM-WC	-0.979	0.987	0.994	-0.269	0.790	-0.258	0.211

8.6   HIGH-FIDELITY SINGLE-OBJECTIVE OPTIMIZATION

In this section, four derivative-free global and hybrid global/local optimization algorithms are presented and applied to a single-objective high-fidelity optimization problem using RANS. Two algorithms are well-known global optimization approaches, specifically (a) the DIRECT (DIviding RECTangles) algorithm [15], and (b) a deterministic version of the particle swarm optimization method (DPSO, [16]). The other two algorithms are hybrid global/local techniques integrated in (a) and (b), respectively, enhancing the global methods with proved stationarity of the final solution. A hybrid DIRECT method coupled with line search-based derivative-free optimization, namely DIRMIN-2 [17], and a hybrid DPSO coupled with line search-based derivative-free optimization, namely LS-DF PSO [18] are presented and applied. The problem is solved using a RANS solver (CFDShip-Iowa v4.5) [6] with a first order polyharmonic spline metamodel [19]. The basis functions for the shape modification are eleven and are the result of a dimensionality reduction analysis, based on the Karhunen–Loève expansion (KLE) [7][20].

8.6.1   Hull-form Optimization Problem

The objective function is the total resistance coefficient (C_T) in calm water at Fr = 0.25. The model scale is considered. Shape modifications $\boldsymbol{\delta}_s$ are produced directly on the Cartesian coordinates $\mathbf{x}_s$ of the computational body surface grid, as per

$$\mathbf{x}_s(\boldsymbol{\alpha}) = \mathbf{x}_{s,0} + \boldsymbol{\delta}_s(\boldsymbol{\alpha}) \tag{2}$$

where $\boldsymbol{\alpha}$ is the design variable vector and $\mathbf{x}_{s,0}$ represents the original body surface grid. An orthogonal expansion of the shape modification vector $\boldsymbol{\delta}_s$ is used, since it is deemed more efficient in the context of shape design optimization [21]. Geometric constraints include fixed length between perpendicular and fixed displacement (∇), with beam (B) and draft (T) varying between ±5% of the original hull. Fixed LBP and ∇ are satisfied by automatic geometric scaling, while constraints for B and T are handled using a penalty function method. This is used here, since the relationship between beam/draft variations and design variables is not explicitly provided by the orthogonal expansion and geometric scaling.

The main particulars of the DTMB 5415 model scale and tests conditions are summarized in Table 8-8 and Table 8-9, respectively.

Table 8-8: DTMB 5415 model main particulars (model scale).

Description	Symbol	Units	Value
Displacement	∇	tonnes	0.549
Length between perpendiculars	LBP	m	5.720
Beam	B	m	0.760
Draft	T	m	0.248
Longitudinal center of gravity	LCG	m	2.884
Vertical center of gravity	VCG	m	0.056

Table 8-9: Test conditions (model scale).

Description	Symbol	Units	Value
Froude number	Fr	-	0.25
Reynolds number	Re	-	$9.82 \cdot 10^6$
Water density	ρ	kg/m^3	998.5
Kinematic viscosity	ν	m^2/s	$1.09 \cdot 10^{-6}$
Gravity acceleration	g	m/s^2	9.803

8.6.2 Design Modification and Dimensionality Reduction Methods

The shape modifications $\boldsymbol{\delta}_s$ is identified using $M = 27$ orthogonal basis functions of the Cartesian coordinates x, y, and z over a hyper-rectangle

$$\boldsymbol{\varphi}_j(x, y, z) : \mathcal{V} = [0, L_x] \times [0, L_y] \times [0, L_z] \in \mathbb{R}^3 \to \mathbb{R}^3, \quad j = 1, \dots, M \tag{3}$$

as

$$\boldsymbol{\delta}_s(x, y, z) = \sum_{j=1}^{M} \beta_j \boldsymbol{\varphi}_j(x, y, z) \tag{4}$$

where the coefficients $\beta_j \in \mathbb{R}$ $(j = 1, \dots, M)$ are the design variables,

$$\boldsymbol{\varphi}_j(x, y, z) := \sin\left(\frac{n_j \pi x}{L_x} + \phi_j\right) \sin\left(\frac{m_j \pi y}{L_y} + \chi_j\right) \sin\left(\frac{l_j \pi z}{L_z} + \theta_j\right) \mathbf{e}_{q(\mathrm{j})} \tag{5}$$

and the following orthogonality property is imposed:

$$\iiint_{\mathcal{V}} \boldsymbol{\varphi}_i(x, y, z) \cdot \boldsymbol{\varphi}_j(x, y, x) dx dy dz = \delta_{i,j} \tag{6}$$

In Eq. (5), n_j, m_j, and $l_j \in \mathbb{R}$, define the order of the function in x, y, and z direction respectively; ϕ_j, χ_j and $\theta_j \in \mathbb{R}$ are the corresponding spatial phases; L_x, L_y and $L_z \in \mathbb{R}$ define the domain size; $\mathbf{e}_{q(j)}$ is a unit vector. Modifications may be applied in x, y, or z direction, with $q(j) = 1, 2,$ or 3 respectively. Table 8-10 summarizes the parameters used herein.

Table 8-10: Orthogonal function parameters for shape modification

j	n_j	ϕ_j	m_j	χ_j	l_j	θ_j	$q(j)$	$\beta_{j,\min}$ (m)	$\beta_{j,\max}$ (m)
1	1.0	0	1.0	0	1.0	0	2	-1.0	1.0
2	1.0	0	1.0	0	2.0	0	2	-1.0	1.0
3	1.0	0	2.0	0	1.0	0	2	-1.0	1.0
4	2.0	0	1.0	0	1.0	0	2	-1.0	1.0
5	1.0	0	2.0	0	2.0	0	2	-1.0	1.0
6	2.0	0	1.0	0	2.0	0	2	-1.0	1.0
7	2.0	0	2.0	0	1.0	0	2	-1.0	1.0
8	2.0	0	2.0	0	2.0	0	2	-1.0	1.0
9	1.0	0	1.0	0	3.0	0	2	-1.0	1.0
10	1.0	0	3.0	0	1.0	0	2	-1.0	1.0
11	3.0	0	1.0	0	1.0	0	2	-1.0	1.0
12	1.0	0	2.0	0	3.0	0	2	-1.0	1.0
13	2.0	0	1.0	0	3.0	0	2	-1.0	1.0
14	1.0	0	3.0	0	2.0	0	2	-1.0	1.0
15	2.0	0	3.0	0	1.0	0	2	-1.0	1.0
16	3.0	0	1.0	0	2.0	0	2	-1.0	1.0
17	3.0	0	2.0	0	1.0	0	2	-1.0	1.0
18	2.0	0	2.0	0	3.0	0	2	-1.0	1.0
19	2.0	0	3.0	0	2.0	0	2	-1.0	1.0
20	3.0	0	2.0	0	2.0	0	2	-1.0	1.0
21	1.0	0	3.0	0	3.0	0	2	-1.0	1.0
22	3.0	0	1.0	0	3.0	0	2	-1.0	1.0
23	3.0	0	3.0	0	1.0	0	2	-1.0	1.0
24	2.0	0	3.0	0	3.0	0	2	-1.0	1.0
25	3.0	0	2.0	0	3.0	0	2	-1.0	1.0
26	3.0	0	3.0	0	2.0	0	2	-1.0	1.0
27	3.0	0	3.0	0	3.0	0	2	-1.0	1.0

The design space modification defined by Eq. (4) is reduced in dimensionality using the generalized KLE method presented in [7]:

$$\boldsymbol{\delta}_s(\xi,\eta) \approx \sum_{j=1}^{N} \alpha_j \boldsymbol{\Phi}_j(\xi,\eta) \tag{7}$$

where ξ and η are curvilinear coordinates over the (demi) hull, $\alpha_j \in \mathbb{R}$ ($j = 1,\ldots,N$) are new design variables and $\boldsymbol{\Phi}_j$ are the solutions of the eigenproblem

$$\iint_S \rho(\xi',\eta') \langle \boldsymbol{\delta}_s(\xi,\eta) \otimes \boldsymbol{\delta}_s(\xi',\eta') \rangle \boldsymbol{\Phi}_j(\xi',\eta') d\xi d\eta = \lambda_j \boldsymbol{\Phi}_j(\xi,\eta) \tag{8}$$

provided that $\langle \boldsymbol{\delta}_s(\xi,\eta,\boldsymbol{\alpha}) \rangle = \mathbf{0}$, $\forall(x,y,x) \in \mathcal{V}$. The brackets $\langle \cdot \rangle$ indicate ensemble average over the realizations of the design variable vector $\boldsymbol{\beta} = \{\beta_j\} \in \mathcal{L}$, which is assessed here using 10,000 uniform random samples (each of them resulting in a modified hull form). The weight $\rho \in \mathbb{R}^+$ defines a generalized inner product and is used to give more emphasis to the submerged grid nodes. The following orthogonality property holds [22][23]

$$\iint_{\mathcal{S}} \rho(\xi,\eta)\mathbf{\Phi}_j(\xi,\eta)\cdot\mathbf{\Phi}_j(\xi,\eta)dxdydz = \delta_{i,j} \qquad (9)$$

Finally, the reduced dimension *N* is selected in order to retain the 90% of the original variability of the geometric variance, as

$$\sum_{j=1}^{N}\lambda_j \geq 0.90\sum_{k=1}^{\infty}\lambda_k \qquad (10)$$

provided that $\lambda_1 \geq \lambda_2 \geq \cdots \geq \lambda_j \geq \lambda_{j+1}$. For the current problem *N*=11 and the corresponding eigenfunctions (represented on the hull) are shown in Figure 8-12. Details of the formulation and numerical implementation of the design space dimensionality reduction technique may be found in [7]. Details of the application to the hull form optimization of the DTMB 5415 may be found in [20].
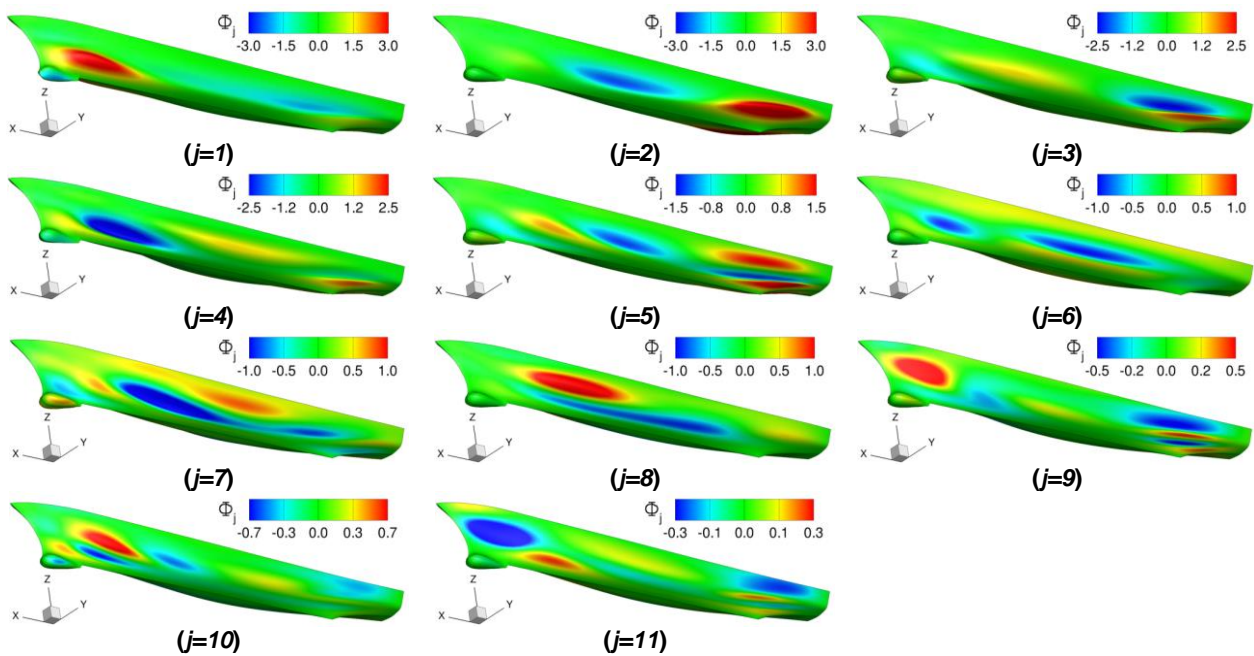

Figure 8-12: KLE solutions Φ_j.

8.6.3 Hydrodynamic Analysis and Metamodelling

RANS simulations are performed with the CFDShip-Iowa v4.5 code, as presented in Section 8.5.2.2. Details about background and boundary layer volume grids can be found in Table 8-4 and Figure 8-3. The boundary layer grid is designed to have $y^+ = 0.3$ at Fr = 0.25.

The optimization problem is solved using a metamodel, trained by 71 RANS simulations defined using a sequential sampling procedure [24]. The metamodel used is a first order polyharmonic spline, which is a special case of radial basis function (RBF) interpolation [19]. For the hull form optimization process, a limit to the number of metamodel-based function evaluations is set equal to 8800, i.e.,800*N*.

8.6.4 Automatic Boundary-layer Grid Modification

The boundary layer (volume) grid is automatically modified, in order to reflect the shape modification applied to the body (surface) grid. Assume that the body surface grid is defined with index $J = 1$ and spanned by indices $I = 1, ..., I_{max}$ and $K = 1, ..., K_{max}$. Accordingly, the boundary layer grid is spanned by $I = 1, ..., I_{max}$, $J = 1, ..., J_{max}$ and $K = 1, ..., K_{max}$, with $J = J_{max}$ corresponding to the outer surface. Once the grid nodes of the body surface at $J = 1$ are modified as per Eq. (7), any arbitrary inner node of the boundary layer grid ($J = 2, ..., J_{max-1}$) is modified similarly to Eq. (2), as

$$\mathbf{x} = \mathbf{x}_0 + \boldsymbol{\delta} \tag{11}$$

with

$$\boldsymbol{\delta} = \frac{l^\star - l}{l^\star} \boldsymbol{\delta}_s + \frac{l}{l^\star} \boldsymbol{\delta}_s^\star \tag{12}$$

where l is the distance between (original) inner and body surface nodes, with arbitrary J and $J = 1$, respectively (and same I and K indices); l^* is the distance between (original) outer and body sur-face nodes, with $J = J_{max}$ and $J = 1$, respectively (and same I and K indices); $\boldsymbol{\delta}_s^\star$ is the modification of the outer surface ($J = J_{max}$):

$$\boldsymbol{\delta}_s^\star = c\boldsymbol{\delta}_s \tag{13}$$

with $c \in \mathbb{R}_0^+$.

The distance l (and l^*) may be evaluated in the simplest form as the Euclidean distance $\overline{l}$:

$$l = \overline{l} = \| \mathbf{x}_0 - \mathbf{x}_{s,0} \| \tag{14}$$

Alternatively, the approximate curvilinear distance $\hat{l}$ along the grid line at constant I and K may be used [25]:

$$l = \hat{l} = \sum_{j=1}^{J-1} \| \mathbf{x}_0^{(j+1)} - \mathbf{x}_0^{(j)} \| \tag{15}$$

where superscripts indicate grid indices, limited to J for the sake of compactness (since I and K are constant). In the current work, $c = 0$ in Eq. (13) and $l = \hat{l}$ in Eq. (12). During the metamodel training, each modified grid is assessed for quality by means of y^+, determinant of the Jacobian matrix and skewness.

8.6.5   Optimization Algorithms

Consider the following objective function:

$$f(\boldsymbol{\alpha}) : \mathbb{R}^N \to \mathbb{R} \tag{16}$$

and the single-objective global optimization problem

$$\min_{\boldsymbol{\alpha} \in \mathcal{L}} f(\boldsymbol{\alpha}), \quad \mathcal{L} \subset \mathbb{R}^N \tag{17}$$

where $\boldsymbol{\alpha} = \{\alpha_j\}$ is the design variable vector and $\mathcal{L}$ is a closed and bounded subset of $\mathbb{R}^N$, identified here by the lower (ℓ_j) and upper (u_j) bounds of each design variable α_j. The global minimization of the objective function $f(\boldsymbol{\alpha})$ requires to find a vector $\mathbf{a} \in \mathcal{L}$ so that:

$$\forall \mathbf{b} \in \mathcal{L} : f(\mathbf{a}) \leq f(\mathbf{b}) \tag{18}$$

Then, $\boldsymbol{\alpha} = \mathbf{a}$ is a global minimum for the function $f(\boldsymbol{\alpha})$ over $\mathcal{L}$. The exact identification of a global minimum might be very difficult, representing a theoretical, methodological, and technological challenge. Therefore, approximate solutions provided by heuristic procedures are often considered acceptable for practical purposes. The deterministic derivative-free global algorithms (DIRECT and DPSO) and their global/local hybridizations (DIRMIN-2 and LS-DF PSO) are presented in the following, for the solution of Eq. (17).

8.6.5.1   The DIRECT Algorithm

DIRECT is a sampling deterministic global derivative-free optimization algorithm and a modification of the Lipschitzian optimization method [15]. It starts the optimization by transforming the search domain $\mathcal{L}$ of the problem into the unit hyper-cube $\mathcal{D}$. At the first step of DIRECT, $f(\boldsymbol{\alpha})$ is evaluated at the center (c) of $\mathcal{D}$; the hyper-cube is then partitioned into a set of smaller hyper-rectangles and $f(\boldsymbol{\alpha})$ is evaluated at their centers. Let the partition of $\mathcal{D}$ at iteration k be defined as $\mathcal{H}_k = \{\mathcal{D}_i : i \in \mathcal{I}_k\}$, with

$$\mathcal{D}_i = \{\boldsymbol{\alpha} \in \mathbb{R}^N : \ell_j^{(i)} \leq \alpha_j \leq u_j^{(i)}, \quad j = 1, \ldots, N, \quad \forall i \in \mathcal{I}_k\} \tag{19}$$

where N is the number of design variables, $\ell_j^{(i)}$ and $u_j^{(i)} \in [0,1]$, with $i \in \mathcal{I}_k$, are the lower and upper bounds defining the hyper-rectangle $\mathcal{D}_i$, and $\mathcal{I}_k$ is the set of indices identifying the subsets defining the current partition. At a generic kth iteration of the algorithm, starting from the current partition $\mathcal{H}_k$ of $\mathcal{D}$, a new partition $\mathcal{H}_{k+1}$, is built by subdividing a set of promising hyper-rectangles of the previous one. The identification of "potentially optimal" hyper-rectangles is based on some measure of the hyper-rectangle itself and on the value of $f(\boldsymbol{\alpha})$ at its center c_i. The refinement of the partition continues until a prescribed number of function evaluations have been performed, or another stopping criterion is satisfied. The minimum of $f(\boldsymbol{\alpha})$ over all the centers of the final partition, and the corresponding center, provide an approximate solution to the problem. It may be noted that the box constraints are automatically satisfied.

8.6.5.2 Local Hybridization of the DIRECT Algorithm: DIRMIN-2

DIRMIN-2 is a global/local hybridization of the DIRECT algorithm and a variant of DIRMIN [26][17]. Differently from DIRMIN, that performs as many local searches as the number of identified potentially optimal hyper-rectangles, DIRMIN-2 performs a single derivative-free local minimization per iteration, starting from the best point produced by dividing the potentially-optimized hyper-rectangles. DIRMIN-2's local minimization is used when the number of function evaluations reaches the activation trigger $\gamma \in (0,1)$, a ratio of the maximum number of function evaluations (N_{fmax}). The local minimization proceeds until either the number of function evaluations exceeds N_{fmax} or the step size Δ falls below a given tolerance β. The local search is not allowed to violate the box constraints. The performance of the algorithm varying the tolerance β and the activation trigger γ has been studied in [17], where DIRMIN-2 is applied to a ship optimization problem. Herein the following setup are used: $\gamma = 0$, $\beta = 10^{-2}$.

8.6.5.3 The DPSO Algorithm

The details about the single-objective deterministic particle swarm optimization algorithm, used in this section, can be found in Chapter 3 and in Ref. [16].

8.6.5.4 Local Hybridization of the DPSO Algorithm: LS-DF PSO

Global convergence properties of a modified PSO scheme may be obtained by properly combining PSO with a line search-based derivative-free method, so that convergence to stationary points can be forced at a reasonable cost. Ref. [18] provides a robust method to force the convergence of a subsequence of points toward a stationary point, which satisfies first order optimality conditions for the objective function. The method, namely LS-DF_PSO, starts by coupling the DPSO scheme with a line search-based method. Specifically, a Positively Spanning Set (PSS) is used, where the set of search directions ($D_{\oplus}$) is defined by the unit vectors $\pm e_i$, $i = 1, ..., N$, as shown in the following equation (i.e., $N = 2$).

$$D_{\oplus} = \left\{ \begin{pmatrix} 0 \\ 1 \end{pmatrix}, \begin{pmatrix} -1 \\ 0 \end{pmatrix}, \begin{pmatrix} 0 \\ -1 \end{pmatrix}, \begin{pmatrix} 1 \\ 0 \end{pmatrix} \right\} \tag{20}$$

After each DPSO iteration, the local search from the best particle is performed if the swarm has not find a new global minimum. The initial step size (ζ_k) for the local search is set equal to 0.25 times the variable domain range, and it is reduced by $\vartheta = 0.5$ at each local search iteration. Local searches continue in each direction until the step size is greater than $\mu = 10^{-3}$. If the local search stops without providing a new global minimum, the actual global minimum is declared as a stationary point. The line search method is not allowed to violate the box constraints.

8.6.6 Numerical Results

A preliminary sensitivity analysis for each design variable is presented in Figure 8-13, showing the associated percent resistance reduction (Δf) with respect to the original hull. The quality of the grids produced by the method presented in Section 8.6.4 is assessed for each modified design. Figure 8-14b presents a modified grid laying on the boundary of the design space, showing an acceptable quality. Non-dimensional design variables are shown in the plots, $x_j = 2(\alpha_j - \ell_j)/(u_j - \ell_j)$. Changes in f are found significant for all variables, revealing a possible reduction of the total resistance at Fr = 0.25 close to 5%.
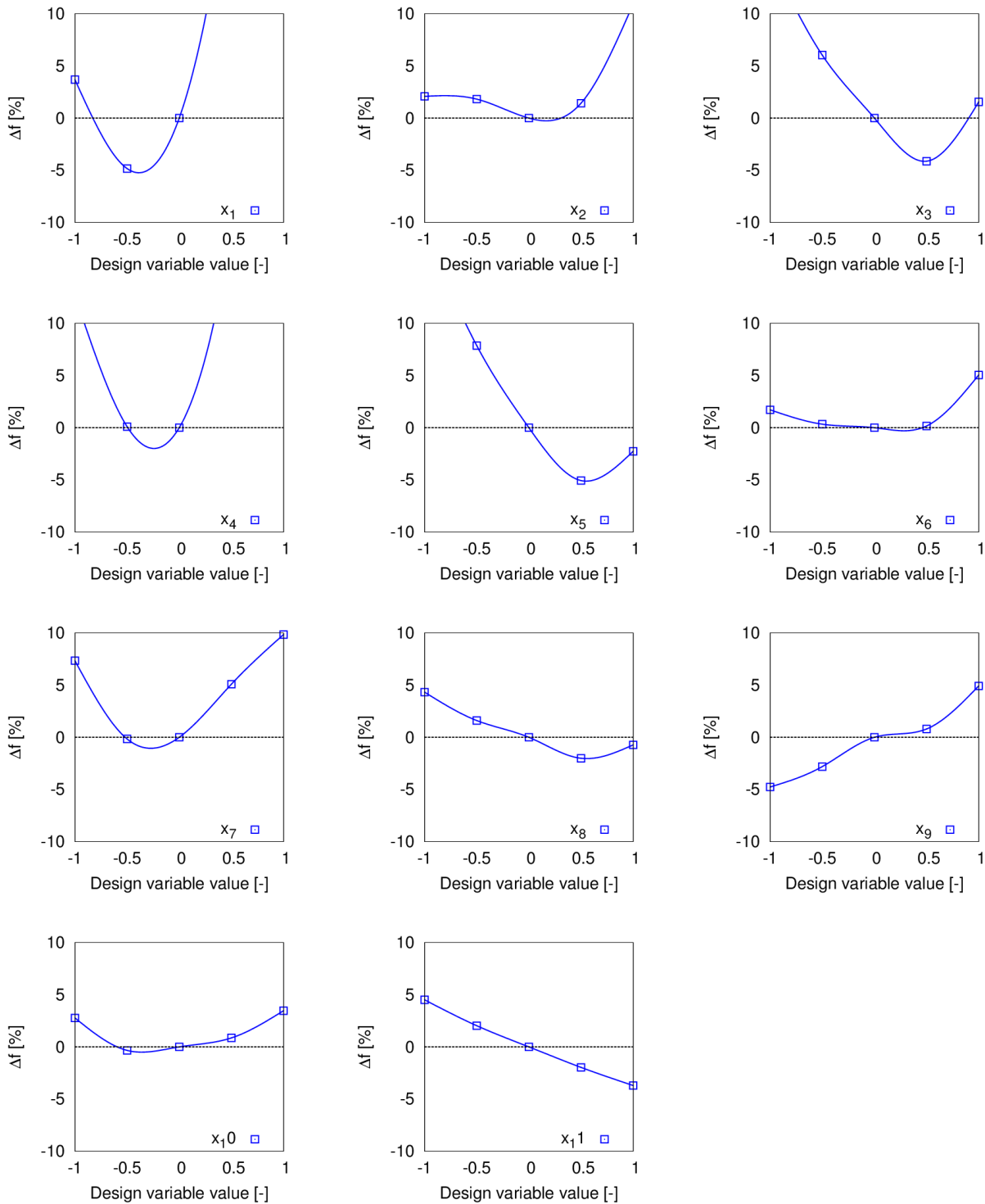
Figure 8-13: Sensitivity analysis of non-dimensional design variables.

(a) Original hull

(b) Modified hull laying on the design space boundary (x_1=1)
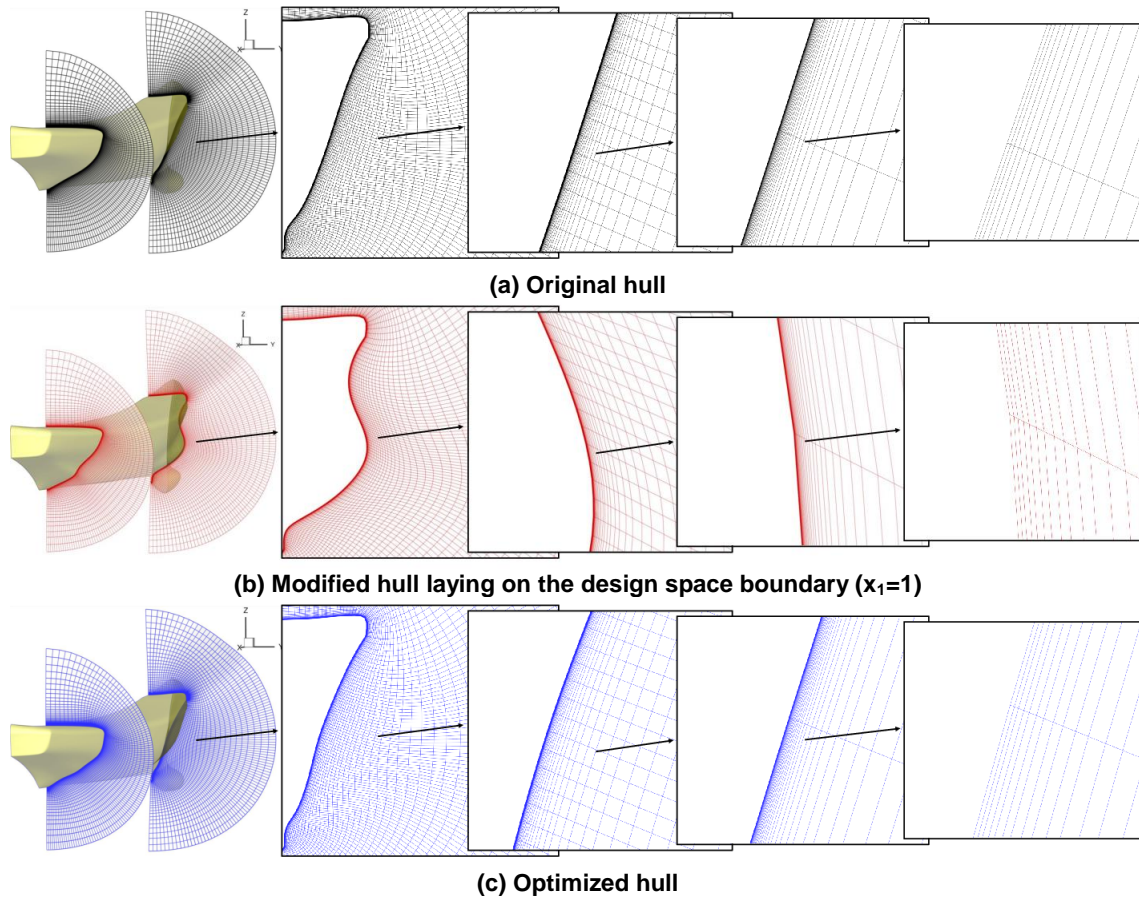
(c) Optimized hull

Figure 8-14: A 5.720 m length model of the DTMB 5415 (CNR-INSEAN model 2340).
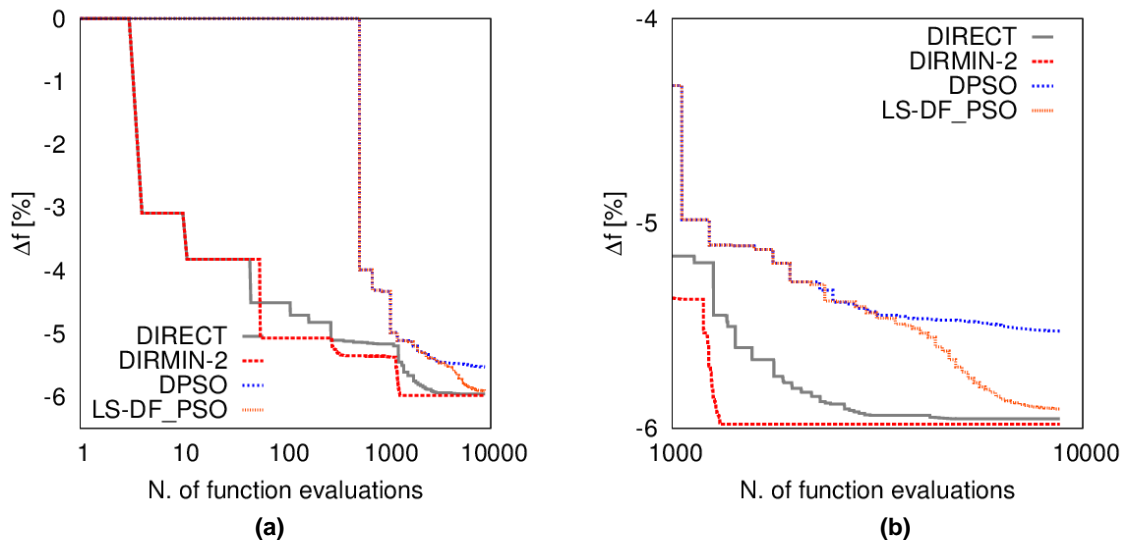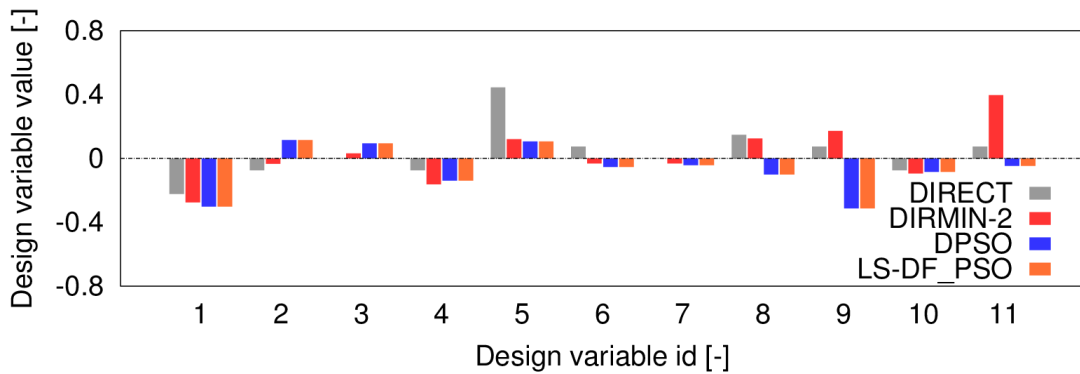

Figure 8-15: Objective function convergence history (a) and detail after the first 1000 function evaluations (b).

The analysis of the results is conducted setting apart results (i) for a low budget of 1100 function evaluations (which corresponds to 100N, an eighth of the full budget), and (ii) for the full budget of 8800 function evaluations (which corresponds to 800N).
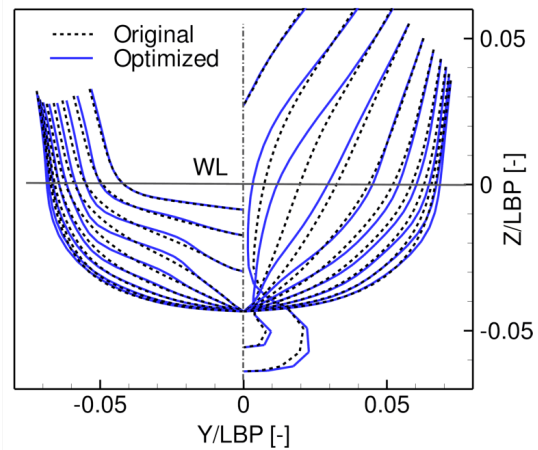
For the case (i), the optimization procedure achieves a total resistance coefficient reduction of 5.16% and 5.37% using DIRECT and DIRMIN-2, respectively, and a reduction of 4.98% using both DPSO and LS-DF PSO. DIRMIN-2 outperform its global version, whereas DPSO and its hybrid reach the same result because non a local search has been activated by LS-DF PSO. DIRMIN-2 is found the most efficient algorithm for the present SBD problem, achieving the best design with the fastest convergence rate, as shown in Figure 8-15. Figure 8-16 presents the values of the optimized design variables, showing appreciable differences, and shows the corresponding optimized shapes, compared to the original.
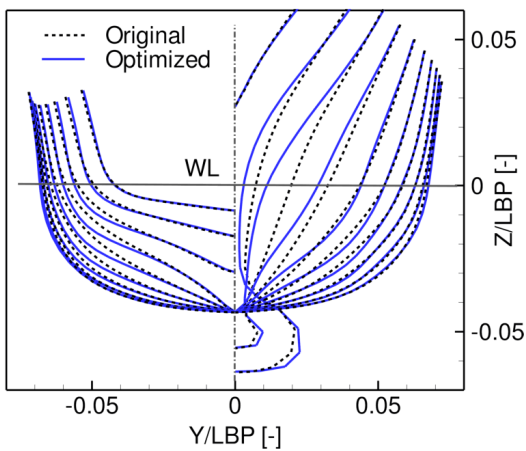

(a) Objective function convergence of optimized design variables
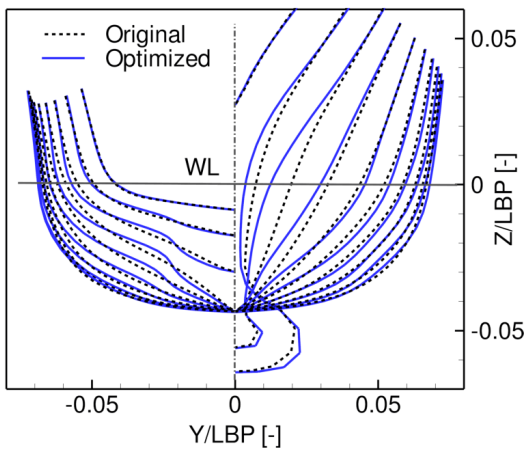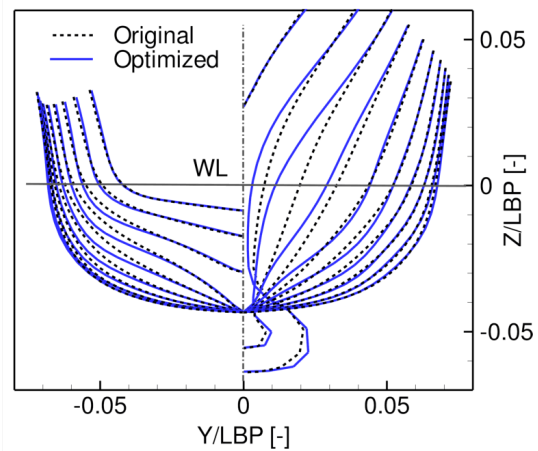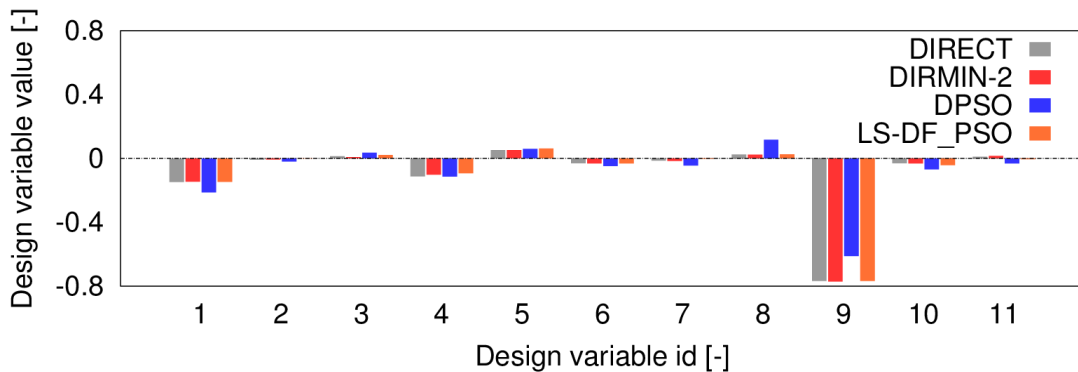

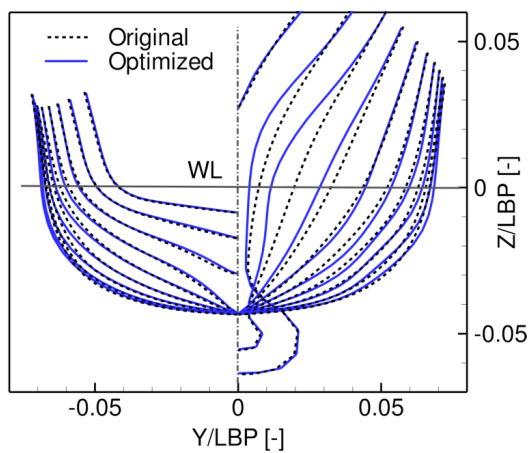
(b) DIRECT

(c) DIRMIN-2

(d) DPSO

(e) LS-DF_PSO

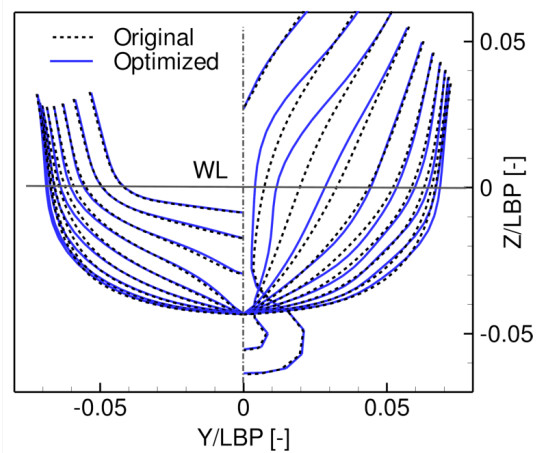Figure 8-16: 1100 function evaluations.

For the case (ii), the optimization procedure achieves a resistance reduction of 5.95% and 5.98% using DIRECT and DIRMIN-2, respectively, and a reduction of 5.52% and 5.91% using DPSO and LS-DF PSO, respectively. The convergence history of the objective function towards the minimum is shown in Figure 8-15, confirming the efficiency and robustness of the two hybrid global/local approaches DIRMIN-2 and LS-DF PSO. More in detail, DIRMIN-2 achieves the most significant reduction of the objective function overall, although all the solutions are very close in this case. Figure 8-17 presents the values of the corresponding optimized design variables and shows the optimized shapes compared to the original.
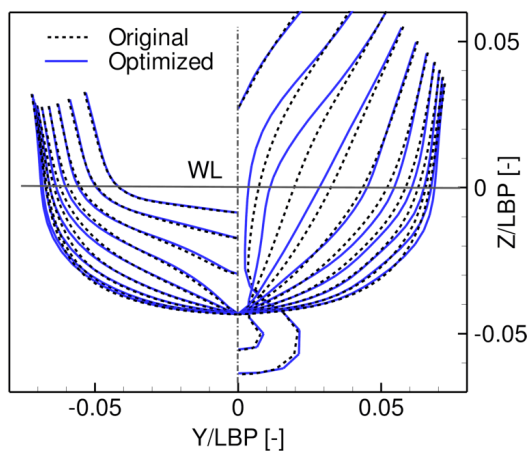

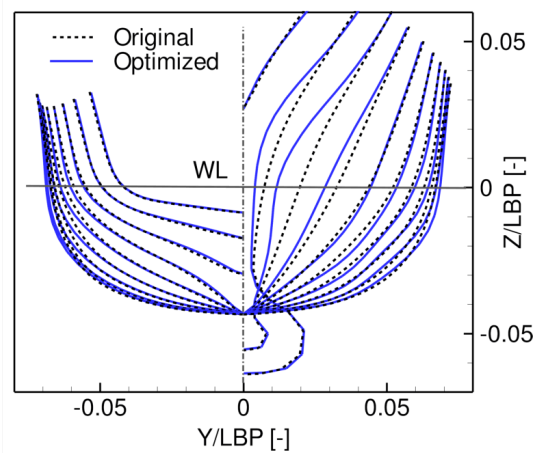(a) Objective function convergence of optimized design variables

(b) DIRECT

(c) DIRMIN-2

(d) DPSO

(e) LS-DF_PSO

Figure 8-17: 8800 function evaluations.

Table 8-11: Summary of the optimization results.

N. funct. eval.	Algorithm	Design variables (non-dimensional)											$C_T(\times 10^{-3})$	
		x_1	x_2	x_3	x_4	x_5	x_6	x_7	x_8	x_9	x_{10}	x_{11}	Value	Δf %
1100	DIRECT	-0.22	-0.07	0.00	-0.07	0.44	0.07	0.00	0.15	0.07	-0.07	0.07	4.00	-5.16
	DIRMIN-2	-0.28	-0.03	0.03	-0.16	0.12	-0.03	-0.03	0.13	0.17	-0.09	0.40	3.99	-5.37
	DPSO	-0.30	0.11	0.09	-0.14	0.11	-0.05	-0.04	-0.10	-0.31	-0.08	-0.05	4.01	-4.98
	LS-DF_PSO	-0.30	0.11	0.09	-0.14	0.11	-0.05	-0.04	-0.10	-0.31	-0.08	-0.05	4.01	-4.98
8800	DIRECT	-0.15	-0.01	0.01	-0.11	0.05	-0.03	-0.01	0.02	-0.77	-0.03	0.01	3.97	-5.95
	DIRMIN-2	-0.15	-0.01	0.01	-0.10	0.05	-0.03	-0.02	0.02	-0.77	-0.03	0.02	3.97	-5.98
	DPSO	-0.21	-0.02	0.04	-0.11	0.06	-0.05	-0.04	0.12	-0.61	-0.07	-0.03	3.99	-5.52
	LS-DF_PSO	-0.15	-0.06	0.02	-0.09	0.06	-0.03	-0.03	0.03	-0.77	-0.04	-0.01	3.97	-5.91

The close agreement of the solutions obtained by the different algorithms indicates that the global minimum region has been likely achieved. A summary of the optimization results is presented in Table 8-11.

The best design is finally assessed with RANS. The associated modified grid is assessed and presented in Figure 8-14c, showing a good quality. The results are presented in Figures 8-18, 8-19, 8-20, and 8-21, and Table 8-12. Figures 8-18 and 8-21 show a significant reduction of the diverging bow wave and a small reduction of the diverging and transverse stern wave. It may be also noted how the shoulder wave is cancelled. Specifically, the optimized shoulder shape induces a high pressure region in correspondence of the first trough of the original hull, causing a phase shift with the reduction of the diverging bow wave and the cancellation of the shoulder wave (well visible in Figure 8-21). This effect has been also shown in retrofitting studies by optimization of blisters attached to the original hull [27]. A longitudinal wave cut along the $y = 0.1$LBP plane is shown in Figure 8-19, highlighting the reduction of the wave elevation, especially at the bow.

Table 8-12: Comparison between original and optimized DTMB 5415 hydrodynamic coefficients (Cpp represent the piezometric pressure, Ch the hydrostatic pressure, Cf the viscous shear stress, Cmg,x the component of the weight force along the longitudinal axis, and CT the total resistance)

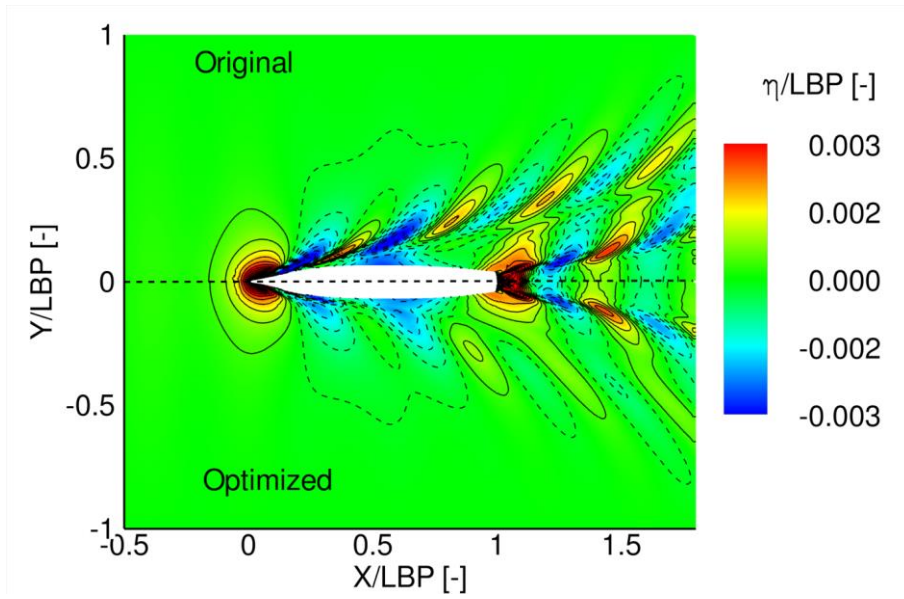| Parameter	Unit	Original	Optimized	Δ%
C_{pp}	-	1.38E-03	9.08E-04	-34.0
C_h	-	0.86E-03	1.24E-03	42.0
C_f	-	3.16E-03	3.18E-03	0.65
$C_{mg,x}$	-	-1.19E-03	-1.35E-03	-13.4
C_T	-	4.21E-03	3.97E-03	-6.00
σ/LBP	-	-1.31E-03	-1.35E-03	-3.29
τ	deg	-0.11	-0.12	-15.3
$S_{w,stat}$/LBP^2	-	1.48E-02	1.50E-02	0.96

Figure 8-18: Wave patterns produced by optimized hull forms at Fr = 0.25 compared with original.
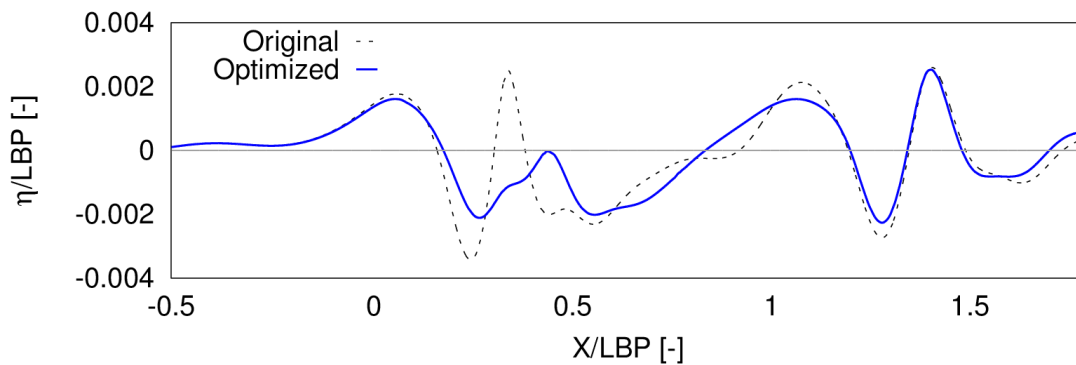

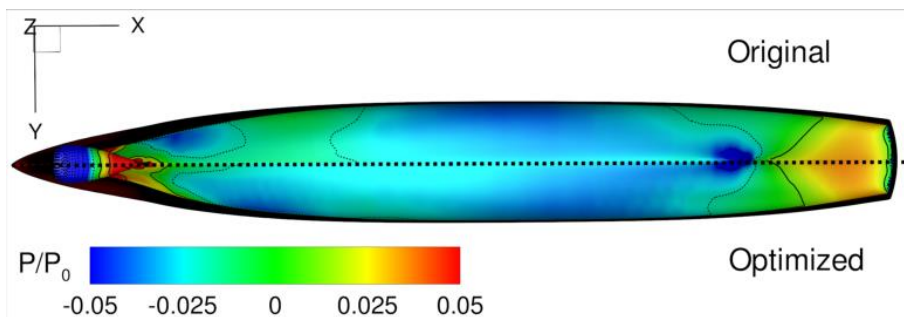**Figure 8-19: Longitudinal wave cut on the y = 0.1 LBP plane at Fr = 0.25 for optimized and original hulls.**

Figure 8-20: Pressure field on optimized hull forms at Fr = 0.25 compared with original.

Finally, Figure 8-20 presents the pressure field on the optimized shape compared to the original shape, showing a more uniform pressure distribution along the hull and a slightly better pressure recovery at the stern. The hydrodynamic coefficients for the original and the optimized hulls are finally compared in Table 8-11, confirming that a large part of the resistance reduction stems from the reduction of the piezometric pressure coefficient.
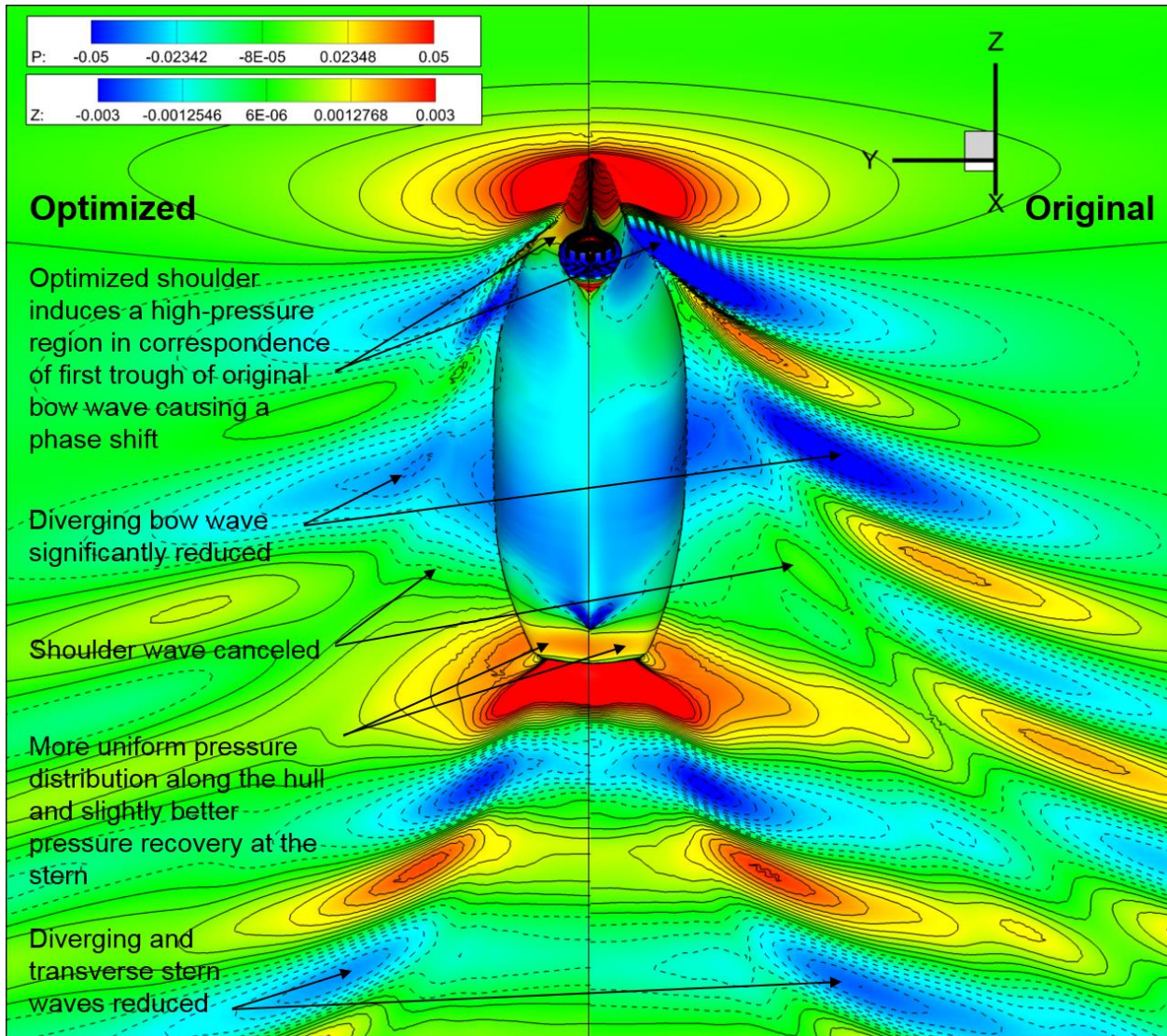

Figure 8-21: Bottom view of wave pattern and pressure distribution at Fr = 0.25 for optimized (left) and original (right) hulls.

8.7 CONCLUSIONS

A multi-objective deterministic SBDO of the DTMB 5415 model has been shown, using four different PF formulations, combining Kelvin and Dawson linearization with a standard pressure integral and the transversal wave cut method for the wave resistance calculation. The optimization aimed at the reduction of the total resistance in calm water at Fr=0.25 and Fr=0.41, using six design variables modifying the hull and the sonar dome. A sensitivity analysis at Fr=0.25 using RANS has been also shown, for comparison and correlation with the PF solutions.

The results have shown the effects of the PF formulation on the SBDO outcomes. Specifically, the Pareto fronts look quite different and the selected optimal designs fall in different region of the design space, depending on the PF formulation used (Figure 8-6 and Figure 8-7). The following considerations can be made: (1) the validation for the original hull shows reasonable trends, but NK-PI for low Fr; (2) DM shows better validation especially for sinkage, compared to NK; (3) NK-PI provides significant resistance reductions at low Fr (likely due to an overestimate of the resistance for the original hull) and more limited improvements at high Fr; (4) NK-WC shows a quite opposite trend; (5) DM-PI indicates more limited (and realistic) improvements, for both low and high Fr; it also shows a limited possibility of improving both objectives at the same time; (6) DM-WC provides more significant resistance reduction at high Fr; (7) overall, the WC method always indicates greater improvements at high Fr than PI, likely due to an overestimate for the resistance of the original hull; (8) NK results seem more affected by the wave resistance estimation method than DM.

These outcomes have motivated further investigations by RANS. Specifically, a sensitivity analysis at Fr=0.25 has been conducted and compared with the PF results. This comparison has shown several differences between PF and RANS solutions. Specifically, none of the PF formulations has shown a reasonable trend for all the design variables, compared to RANS. More in detail, DM-PI, NK-WC, DM-WC, and NK-PI show an average absolute error of 2.0, 2.2, 6.8, and 53.0% respectively (see Table 8-6). The analysis of the Pearson's correlation coefficient between PF and RANS results (see Table 8-7) shows a good correlation between NK-PI and RANS for four out of six variables. For the current test case, NK-PI is the more effective PF formulation.

The present work has shown a comparison of low- and high-fidelity solver and how the use of low-fidelity solvers in a hull-form optimization problem can lead to inaccurate design solutions. For this reason, a further deterministic derivative-free RANS-based single-objective optimization of the DTMB 5415 has been performed, using global/local hybridization by derivative-free line search methods of two well-known global algorithms, DIRECT and DPSO, respectively. The optimization has been performed aiming at the reduction of the model scale total resistance coefficient in calm water at Fr = 0.25. The design space has been generated by a linear expansion of orthogonal basis functions for the modification of the hull form. The problem has been solved with a number of design variables equal to eleven. A resistance reduction of 6% has been achieved by the optimized design. The RANS-based optimization relies on more accurate high-fidelity hydrodynamic analyses and provides a more realistic hull form. The final shape obtained with RANS induces a high pressure region in correspondence of the first trough of the diverging bow wave of the original hull. This causes a phase shift with a significant reduction of the bow wave and the cancellation of the shoulder wave. As a result, the pressure distribution appears more uniformly distributed along the hull and most of the resistance reduction stems from the piezometric pressure coefficient.

The hybrid methods reach convergence using about 1100 function calls, whereas the original algorithms seem to need more than 10,000 evaluations to reach convergence. This motivates the use (as in the present study) of metamodels to reduce the computational cost. Nevertheless, latest studies [28] have shown the solution of a stochastic multi-objective optimization of a high-speed catamaran, using a number of 780 RANS simulations in calm water and 1170 in regular waves, with a grid size of 6.9M. This demonstrates the technological possibility of applying directly the optimization algorithm to RANS simulations, even if the

number of function calls becomes larger than 1000, as in the present work. In this case, the efficiency of the optimization algorithm is a crucial issue and (in view of current results) hybrid methods may represent a viable and valid option.

In conclusion, the present research has finally shown how global/local hybridization methods, namely DIRMIN-2 and LS-DF PSO, out-perform their original global algorithms, DIRECT and DPSO. This result has been found significant especially for low budgets of function evaluations. Hybrid algorithms have shown their capability to combine effectively the characteristics of global and local approaches, resulting in a faster (and computationally less expensive) convergence towards the global minimum. This, along with their derivative-free formulation and implementation, makes the present local hybridization methods a viable and effective option for SBD optimization, especially when computationally expensive objective functions are involved. The final hydrodynamic assessment of the RANS-based optimized shape has confirmed the effectiveness of the SBD optimization procedure, driven by hybrid global/local methods.

Future work will focus on the stochastic optimization of the DTMB 5415 hull form, subject to real ocean environment and operations. In this context, the extension of hybrid global/local methods to multi-objective problems will be addressed and combined with metamodel-based optimization by adaptive sampling procedures [24]. Alternatively, multi-fidelity approximations may be used, combining the computational cost of low-fidelity evaluations with the accuracy of high-fidelity simulations [29].

8.8   ACKNOWLEDGEMENTS

8.9   REFERENCES

[1] Chen X., Diez M., Kandasamy M., Zhang Z., Campana E.F., Stern F., "High-fidelity global optimization of shape design by dimensionality reduction, metamodels and deterministic particle swarm." Engineering Optimization 47(4) (2015):473-494.

[2] Kandasamy M., Peri D., Tahara, Y., Wilson W., Miozzi M., Georgiev S., Milanov E., Campana E.F., Stern F., "Simulation based design optimization of waterjet propelled Delft catamaran." International Shipbuilding Progress 60(1)(2013):277–308.

[3] Bassanini P., Bulgarelli U., Campana E.F., Lalli F., "The wave resistance problem in a boundary integral formulation." Surv. Math. Ind. 4 (1994): 151-194.

[4] Telste J.G., Reed A.M., "Calculation of Transom Stern Flows." In Proc. 6th International Conference on Numerical Ship Hydrodynamics (1994): 78-92.

[5] Pellegrini R., Campana E.F., Diez M., Serani A., Rinaldi F., Fasano G., Iemma U., Liuzzi G., Lucidi S., Stern F., "Application of derivative-free multi-objective algorithms to reliability-based robust design optimization of a high-speed catamaran in real ocean environment." In Proc. EngOpt2014 - 4th international conference on engineering optimization Lisbon (8-11 Sept. 2014).

[6] Huang J., Carrica P., Stern F., "Semi-coupled air/water immersed boundary approach for curvilinear dynamic overset grids with application to ship hydrodynamics." Int. J. Numer. Meth. Fluids 58 (2008):

591–624.

[7] Diez M., Campana E.F., Stern F., "Design-space dimensionality reduction in shape optimization by Karhunen–Loève expansion." Computer Methods in Applied Mechanics and Engineering 283 (2015): 1525–1544.

[8] Serani A., Fasano G., Liuzzi G., Lucidi G., Iemma U., Campana E.F., Diez M., "Derivative-free global design optimization in ship hydrodynamics by local hybridization." In Proc. 14th International Conference on Computer Application and Information Technology in the Maritime Industries (COMPIT 2015), Ulrichshusen, Germany, 11-13 May 2015: 331-342.

[9] Serani A., Campana E.F., Diez M., Stern F., "A Multi-Objective Optimization: Effects of Potential Flow Formulation and RANS." In Proc. 15th International Conference on Computer Application and Information Technology in the Maritime Industries (COMPIT 2016), Lecce, Italy, 9-11 May 2016: 8-18.

[10] Serani A., Fasano G., Liuzzi G., Lucidi S., Iemma U., Campana E.F., Stern F., Diez M., "Ship hydrodynamic optimization by local hybridization of deterministic derivative-free global algorithms." Applied Ocean Research 59 (2016) 115-128.

[11] Stern F., Longo J., Penna R., Olivieri A., Ratcliffe T., Coleman H., "International collaboration on benchmark CFD validation data for surface combatant DTMB model 5415." Proceedings of the Twenty-Third Symposium on Naval Hydrodynamics, Val de Reuil, France, September 17-22 (2000).

[12] Dawson C.W., "A practical computer method for solving ship-wave problems." In: Proceedings of the 2nd International Conference on Numerical Ship Hydrodynamics, Berkeley, (1977): 30–38.

[13] Schlichting H., Gersten K., "Boundary-Layer Theory", Springer-Verlag, Berlin (2000).

[14] Olivieri A., Pistani F., Avanzini A., Stern F., Penna R., "Towing tank, sinkage and trim, boundary layer, wake, and free surface flow around a naval combatant INSEAN 2340 model." Tech. rep., DTIC Document (2001).

[15] Jones D., Perttunen C., Stuckman B., "Lipschitzian optimization without the Lipschitz constant." J. Optim. Theory Appl. 79 (1) (1993) 157–181.

[16] Serani A., Leotardi C., Iemma U., Campana E.F., Fasano G., Diez M., "Parameter selection in synchronous and asynchronous deterministic particle swarm optimization for ship hydrodynamics problems." Applied Soft Computing 49 (2016): 313-334.

[17] Campana E.F., Diez M., Iemma U., Liuzzi G., Lucidi S., Rinaldi F., Serani A., "Derivative-free global ship design optimization using global/local hybridization of the DIRECT algorithm." Optim. Eng. 17 (1) (2015)127–156.

[18] Serani A., Diez M., Campana E.F., Fasano G., Peri D., Iemma U., "Globally convergent hybridization of particle swarm optimization using line search-based derivative-free techniques." in: X.-S. Yang (Ed.), Recent Advances in Swarm Intelligence and Evolutionary Computation, Studies in Computational Intelligence, vol. 585, Springer International Publishing, 2015, pp. 25–47.

[19] Volpi, S., Diez, M., Gaul, N.J., Song, H., Iemma, U., Choi, K.K., Campana, E.F., Stern, F., "Development and validation of a dynamic metamodel based on stochastic radial basis functions and

uncertainty quantification." Structural and Multidisciplinary Optimization 51(2), 347–368 (2015).

[20] Diez M., Serani A., Campana E.F., Volpi S., Stern F., "Design space dimensionality reduction for single- and multi-disciplinary shape optimization." in: AIAA/ISSMO Multidisciplinary Analysis and Optimization (MA&O), AVIATION2016, Washington, DC, USA, June 13–17, 2016.

[21] Diez M., Serani A., Campana E.F., Goren O., Sarioz K., Danisman D.B., Grigoropoulos G., Aloniati E., Visonneau M., Queutey P., Stern F., "Multi-objective hydrodynamic optimization of the DTMB 5415 for resistance and seakeeping." in: Proceedings of the 13th International Conference on Fast Sea Transportation, FAST 2015, Washington, DC, USA, 2015.

[22] Iemma U., Morino L., Diez M., "Digital holography and Karhunen–Loève decomposition for the modal analysis of two-dimensional vibrating structures." J. Sound Vib. 291 (1) (2006) 107–131.

[23] Iemma U., Diez M., Morino L., "An extended Karhunen–Loève decomposition for modal identification of inhomogeneous structures." J. Vib. Acoust. 128(2006) 357.

[24] Diez M., Volpi S., Serani A., Stern F., Campana E.F., "Simulation-based design optimization by sequential multi-criterion adaptive sampling and dynamic radial basis functions.", In: EUROGEN 2015, International Conference on Evolutionary and Deterministic Methods for Design, Optimization and Control with Applications to Industrial and Societal Problems, Glasgow, UK, September, (2015).

[25] Paik K.-J., Carrica P.M., Lee D., Maki K., "Strongly coupled fluid-structure interaction method for structural loads on surface ships." Ocean Eng. 36(17–18) (2009) 1346–1357.

[26] Lucidi S., Sciandrone M., "A derivative-free algorithm for bound constrained optimization." Comput. Optim. Appl. 21 (2) (2002) 119–142.

[27] Kandasamy M., Wu P., Zalek S., Karr D., Bartlett S., Nguyen L., Stern F., "CFD based hydrodynamic optimization and structural analysis of the hybrid ship hull." in: SNAME Trans., 2014.

[28] Diez M., Campana E.F., Stern F., "Development and evaluation of hull-form stochastic optimization methods for resistance and operability." in: Proceedings of the 13th International Conference on Fast Sea Transportation, FAST 2015, Washington, DC, USA, 2015.

[29] Pellegrini R., Leotardi C., Iemma U., Campana E.F., Diez M., "A Multi-Fidelity Adaptive Sampling Method for Metamodel-based Uncertainty Quantification of Computer Simulations." To be presented at European Congress on Computational Methods in Applied Sciences and Engineering - ECCOMAS 2016, 5-10 June, Crete Island, Greece (2016).